ELSEVIER

Chemical Engineering Science 61 (2006) 2843–2851

Chemical Engineering Science

www.elsevier.com/locate/ces

Direct numerical simulation of turbulent particle dispersion in an unbaffled stirred-tank reactor

Fabio Sbrizzai[a], Valentina Lavezzo[a], Roberto Verzicco[b], Marina Campolo[a], Alfredo Soldati[a,*,1]

[a]*Dipartimento di Energetica e Macchine, Centro Interdipartimentale di Fluidodinamica e Idraulica,Università di Udine 33100, Udine, Italy*
[b]*Dipartimento di Ingegneria Meccanica e Gestionale and Centre of Excellence for Computational Mechanics (CEMeC) - Politecnico di Bari - 70125, Bari, Italy*

Received 17 June 2005; received in revised form 21 October 2005; accepted 22 October 2005
Available online 18 January 2006

Abstract

Turbulent dispersion of inertial particles in a flat-bottom stirred-tank reactor equipped with an eight-blade Rushton impeller is investigated using accurate numerical techniques (Verzicco et al., 2004, Flow in an impeller-stirred tank using an immersed-boundary method. A.I.Ch.E. Journal, 50(6), 1109–1118.). Direct Numerical Simulation of the turbulent flow field in the vessel is obtained using a second-order finite-difference scheme coded in a cylindrical reference frame, and an immersed-boundary approach is used to simulate the motion of the impeller. The flow scales are resolved explicitly down to the Kolmogorov scale. To give a comprehensive picture of the turbulence structure in the vessel, angle-resolved averages of turbulent kinetic energy, turbulent energy dissipation rate and Kolmogorov time-scales are evaluated in vertical planes aligned with the blade and mid-way between two blades. The dispersion of heavy particles of different diameter is then investigated by Lagrangian tracking. The particle-to-fluid mass loading ratio is low enough to assume one-way coupling momentum transfer between continuous and dispersed phase. Three sets of particles, characterized by different response time, are investigated and, for each set, two equal, randomly distributed swarms are initially released above and below the impeller, which is placed mid-way between top and bottom of the tank. Statistics calculated after 3 impeller revolutions are used to evaluate the evolution of particle dispersion in the flow and to quantify their preferential accumulation into specific regions of the tank.

Keywords: Stirred-tank reactors; DNS; Lagrangian tracking; Turbulence scales

1. Introduction

In a number of industrial applications such as polymerization, solid suspensions, particle coating processes and biotechnologies, solid particles must be dispersed homogeneously in a liquid phase so that optimal process parameters can be met. In many cases, mixing is achieved in vessels—stirred-tank reactor (STR)—in which an impeller generates a flow field characterized by high turbulence levels.

Flow circulation and turbulence in the vessel control transport, dispersion and segregation of particles in the fluid determining the homogeneity of the mixing between phases achieved in the stirring process. Despite the key role of local particle dynamics in the dispersion process, a full understanding of the interaction between turbulence structures and different size particles dispersed in an STR is still lacking. The dispersion process is strongly time-dependent and characterized by a number of mutually interacting, yet different flow scales, which are not equally effective in advecting and dispersing particles. Identifying the scales which produce the largest dispersion within the STR is a crucial information for industrial design, and it is not clear whether the smaller Kolmogorov scales play or not a significant role in the dispersion process.

Particle dispersion in STRs was investigated adopting a Lagrangian approach in the limit of the point-wise particle model by Campolo et al. (2003) and by Derksen (2003). In Campolo et al. (2003) the flow field was computed using time-dependent Reynolds averaged Navier–Stokes simulations (RANS), whereas in Derksen (2003) the flow field was

* Corresponding author. Tel.: +39 432 558020; fax: +39 432 558027.
E-mail address: soldati@uniud.it (A. Soldati).
[1] Also affiliated with Department of Fluid Mechanics, CISM, 33100, Udine, Italy.

0009-2509/$ - see front matter © 2005 Elsevier Ltd. All rights reserved.
doi:10.1016/j.ces.2005.10.073

computed by large eddy simulation (LES). In both RANS and LES approaches, turbulent fluctuations at scales smaller than the grid size are filtered out and models are used to reproduce their effect. Thus, in both works, results for particle dispersion are limited to the analysis of influence of the larger scale structures. To obtain a more faithful representation of the influence of the smaller scales on particle dispersion, sub-grid models *for particle dynamics* should be used. These sub-grid models, however, have not been developed or used broadly so far (Kuerten and Vreeman, 2005; Shotorban and Mashayek, 2005).

A numerical approach which requires no model in the limit of the point-wise particle approximation is based on direct numerical simulation (DNS) of the turbulence which is currently applied only to simple geometries (Rouson and Eaton, 2001; Marchioli and Soldati, 2002; Soldati, 2005). Recently, one DNS of the turbulent flow field in a STR has been published by Verzicco et al. (2004). The authors have shown that, due to the low Reynolds number and to the strongly unsteady and inhomogeneous nature of the flow, RANS perform poorly not achieving accurate estimates of turbulence related quantities—turbulent kinetic energy, turbulent energy dissipation rate and stresses. According to previous works in simplified geometries (Rouson and Eaton, 2001; Marchioli and Soldati, 2002; Picciotto et al., 2005), these quantities play a very important role in particle dynamics, since particles are known to accumulate preferentially into high strain, low-vorticity regions, especially when the particle time-scale and the flow time-scale are of the same order (Wang and Maxey, 1993; Eaton and Fessler, 1994). Therefore, to obtain accurate information on local phenomena like particle segregation, we must rely on numerical approaches which are able to reproduce precisely turbulence related quantities.

In this work, we investigated numerically particle dispersion by (i) solving accurately the balance equation for the fluid up to the Kolmogorov scale and (ii) using a Lagrangian approach to track swarms of particles in the calculated flow field.

Basing on the methodology and on the results of Verzicco et al. (2004), the objects of our research are (i) to build a database which may be useful to test LES and RANS computations, including turbulent quantities modeled by these approaches, i.e., turbulent kinetic energy, turbulent energy dissipation rate and turbulence time-scales; (ii) to identify the role of different size and time-scale flow structures in dispersing particles within the reactor.

We use the finite-difference second-order accurate code described in Verzicco et al. (2004) to solve the Navier–Stokes equations and we model the impeller rotation using the immersed-boundaries approach (Fadlun et al., 2000). Dispersion of particles of 30, 50 and 100 μm diameter is simulated by means of Lagrangian tracking. Although computationally expensive—calculation of particle position and velocity is made for each particle, at each time-step—this is an easy to code and natural approach to understand dispersion processes. Furthermore, since we solve explicitly all the flow scales down to the Kolmogorov scale, no sub-grid model is required to simulate accurately particle dynamics.

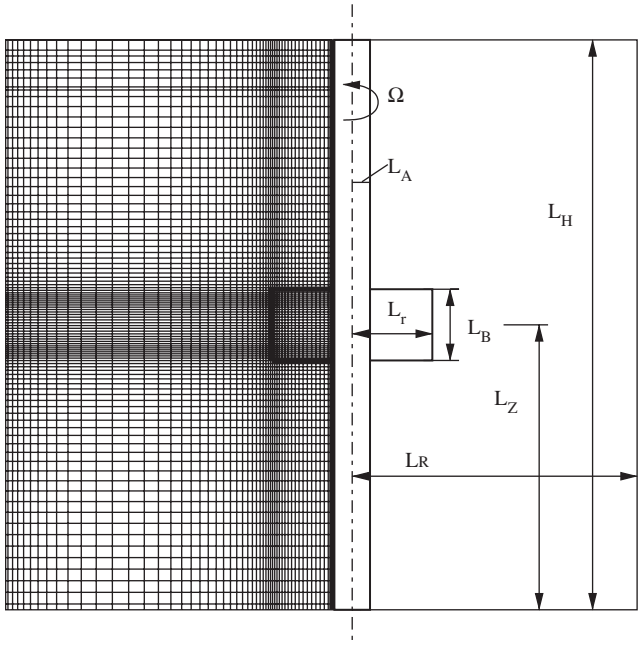

Fig. 1. Geometric dimensions and computational grid used for flow field simulation. Only one grid line for every four is shown in this figure.

2. Methodology

2.1. Fluid flow

Navier–Stokes equations are solved in a cylindrical reference frame for the reactor geometry shown in Fig. 1. The computational domain is discretized into 97 × 102 × 192 (about two millions) grid points in the azimuthal, radial and axial directions, respectively. The mesh (see the left side of Fig. 1) is non-uniform in the radial and axial directions, and is refined selectively in the regions where higher velocity gradients are expected. Specifically, refinements are made in the blade region and close to the shaft (see Verzicco et al., 2004 for a more detailed description).

Dimensions of vessel/impeller—shown in the right side of Fig. 1—made dimensionless using the impeller radius $L_r = 1.25$ cm are: $L_r = 1$, $L_B = 0.8$, $L_A = 0.32$, $L_R = 4$, $L_Z = 4$ and $L_H = 8$. Impeller rotation velocity Ω is equal to 100 rpm. Reference time-scale and velocity are the rotation time, $1/\Omega$, and the blade tip velocity, $U_T = \Omega L_r$. Fluid is water, with density $\rho = 10^3\,\mathrm{kg/m^3}$ and kinematic viscosity $\nu = 10^{-6}\,\mathrm{m^2/s}$. The Reynolds number, based on blade radius and blade tip velocity, $Re = \Omega L_r^2/\nu$, is 1636. Boundary conditions are (i) no-slip at impeller blades and at external walls (enforced using the immersed boundary method) and (ii) free-slip at the top surface to mimic the presence of a flat free surface between water and upper air. As estimated by Verzicco et al. (2004), the free surface deformation is small and should not influence the overall (and local) evolution of the flow field justifying the assumption of a flat, stress-free upper boundary condition.

2.2. Kolmogorov scales

To investigate accurately particle–turbulence interactions, turbulent fluctuations should be explicitly resolved down to the Kolmogorov scales. This implies that space and time resolution for the flow must be chosen accordingly. Following Kolmogorov assumptions (Kolmogorov, 1941), the order of magnitude of space and time-scales for statistically steady turbulence at a given Reynolds number can be evaluated as a function of the fluid kinematic viscosity, v, and of the turbulence-energy dissipation rate, ε. As discussed in Derksen (2003), we assume that the relevant scales at which energy is introduced in the flow are the blade radius, L_r and the blade tip velocity, ΩR. Therefore, the Kolmogorov length scale can be calculated as $\eta/L_r = Re^{-3/4} = 48.5\,\mu\text{m}$ and the Kolmogorov time-scale as $\tau = 1/\Omega\, Re^{-0.5} = 2.35 \times 10^{-3}\,\text{s}$. These values have been used in this work (i) to assess the grid resolution and (ii) to evaluate time resolution required for the flow field calculations. Specifically, in our computational domain, minimum values of grid spacing are $\Delta r = 144\,\mu\text{m}$, $\Delta\theta = 416\,\mu\text{m}$, and $\Delta z = 169\,\mu\text{m}$. These values are 3, 8 and 3.5 times larger than the estimated Kolmogorov spatial scale, respectively. These values would reduce further if other references are used (Pope, 2000) thus confirming our choice for the grid resolution. The time step used for flow field calculation is $\Delta t = 1.25 \times 10^{-4}\,\text{s}$, i.e., about 1/18 of the Kolmogorov time scale. We started our calculation from the flow field obtained by Verzicco et al. (2004), corresponding to a fully developed turbulent flow. The flow field was seeded with particles, randomly dispersed and initially moving at the same velocity of the fluid, and Lagrangian tracking was performed for a time window corresponding to three impeller revolutions. Current computational capabilities did not allow us to extend the simulation time further, and a posteriori analysis showed that this time window is not long enough to obtain a fully developed dispersion field for particles. Therefore, the preliminary results currently available are used to derive information on the transient of dispersion dynamics. Long-term evaluation of particle dispersion will be the object of further investigations.

2.3. Lagrangian tracking

We simulate the dispersion of solid particles considering a swarm made of $O(10^4)$ particles. We calculate the trajectory of each particle by integrating explicitly over time the equation of motion. The assumptions for particle modeling are: (i) all particles are point-wise, non-interacting, non-deformable solid spheres; (ii) particle density is large compared to fluid density; (iii) the effect of the particles on the flow is neglected. As discussed in Section 2.2, the minimum grid spacing is large enough to assume that the point-wise particle approximation is valid.

Particle dynamics is controlled by the Stokes number, St, which is defined as the ratio between the particle response time and the relevant flow time-scale. According to many previous works (see, for instance, Chung and Troutt, 1988; Loth, 2000; Campolo et al., 2005), the study of the order of magnitude of the forces acting on particles based on the equation of motion derived by Maxey and Riley (1983) reveals that the drag force is $O(St^{-1})$, the virtual mass and the pressure gradient are $O(\rho/\rho_p)$ and the Basset force is $O(\rho/\rho_p)^{1/2}$, where ρ and ρ_p are fluid density and particle density, respectively. In our work, $\rho/\rho_p = 0.2 = O(10^{-1})$ and, as shown in Table 1, $St_k = \tau_p/\tau$—that is the Stokes number based on the reference Kolmogorov time-scale for the fluid—is in the range $[10^{-1} - 10^{1}]$. Therefore, for the specific flow system examined here, the equation of motion reduces to a balance of Stokes drag, gravity forces and particle inertia and can be written as

$$m_p \frac{\mathrm{d}\vec{v}_p}{\mathrm{d}t} = \vec{F}_D + \vec{F}_g, \tag{1}$$

where $\vec{F}_D$ and $\vec{F}_g$ are drag and gravity forces, respectively. Eq. (1) was integrated using a time-step sufficiently small to follow accurately curved trajectories. Specifically, the time resolution of the flow field was chosen equal to one half of the characteristic time of the smallest particle.

Table 1
Particle characteristic time τ_p, dimensionless characteristic time τ_p^* and Stokes number (referred to the estimated Kolmogorov time-scale, $\tau_k = 2.35 \times 10^{-3}$) for three particle diameters used in Lagrangian tracking

Particle diameter d_p(μm)	τ_p(s)	τ_p^*	St_k
30	2.50×10^{-4}	2.62×10^{-3}	0.106
50	6.94×10^{-4}	7.27×10^{-3}	0.295
100	2.78×10^{-3}	2.91×10^{-2}	1.183

3. Results

3.1. Fluid flow

Figs. 2(a) and (b) show the instantaneous flow field in two vertical sections of the reactor, taken mid-way between and one degree behind the impeller blades (i.e., the plane containing the backward face of the impeller blade). Vectors represent radial and axial components of velocity in the plane. We observe that the discharge jet is issued radially from the impeller blade tip. The jet is strong in the close vicinity of the impeller with its momentum decreasing within $r \cong 2L_r$ due to the presence of the side wall. At this location, the jet splits into two axial streams, respectively upward and downward, which form two main circulations corresponding to the upper and lower toroidal vortices. Observing Fig. 2(b), we can further notice that, when it leaves the blade, the axis of the jet is slightly inclined upward due to the different boundary conditions imposed at the bottom (no-slip wall) and at the top (free-slip wall) of the vessel.

The region around the impeller, i.e., the near-field of the discharge jet, is characterized by large velocity fluctuations (figure not shown here). These are crucial features for analysis of dispersion, since velocity fluctuations control the flow at

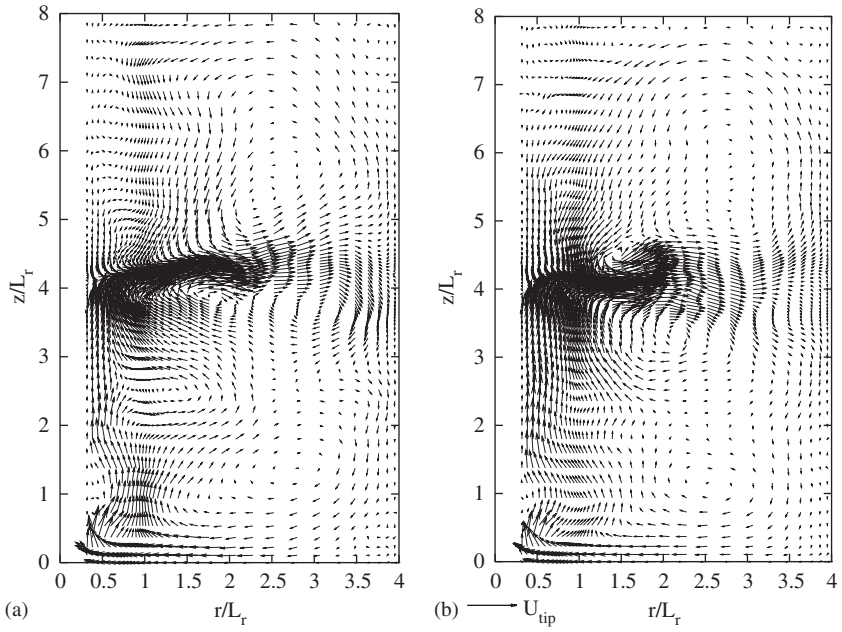

Fig. 2. Instantaneous velocity flow field: (a) 1° behind the impeller blade and (b) vertical plane between two blades.

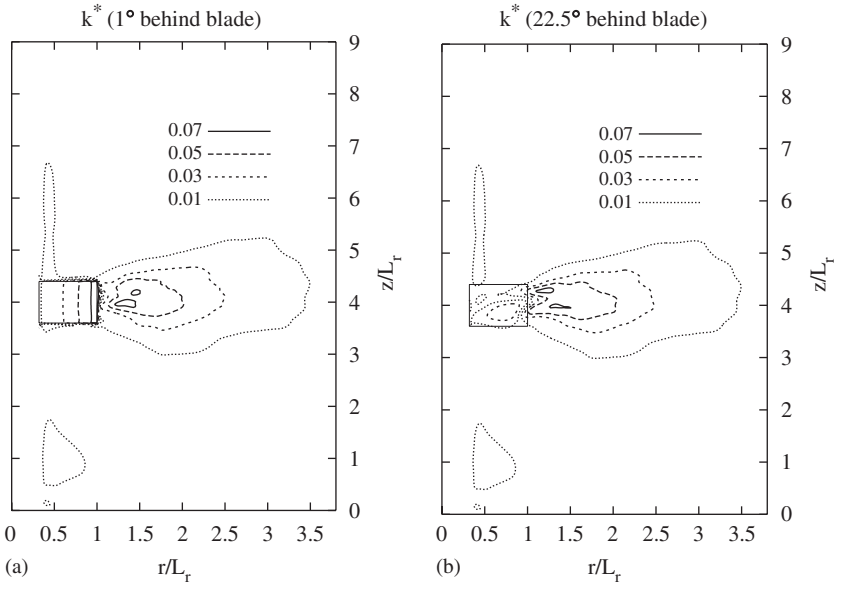

Fig. 3. Isocontours of angle-resolved averages of turbulent kinetic energy. Values are made dimensionless using the reference velocity scale $k^* = k/(\Omega L_r)^2$. Vertical sections are taken (a) 1° behind the impeller blade, and (b) mid-way between two blades.

the micro-scale, contribute to energy dissipation and to many rate-limiting phenomena acting at the same scale (Derksen and Van den Akker, 1999). In this paper, we chose to focus the discussion of results on turbulent kinetic energy and turbulent dissipation rate, since these quantities may represent a useful benchmark for RANS and LES calculations. We refer to the paper by Verzicco et al. (2004) for different statistics.

Fig. 3 shows the angle-resolved averages of the spatial distribution of turbulent kinetic energy obtained for two meridional planes taken (a) one degree behind the impeller blade and (b) 22.5° behind the impeller blade, i.e., mid-way between two blades. Dimensionless values of k were calculated as $k^* = k/(\Omega^2 L_r^2)$. The highest values of turbulent kinetic energy are found at the blade tip, 1° behind the blade. Values of k^* reduce progressively in the impeller region moving toward the side wall (see Fig. 3(a) and (b)) and, in the region above and below the impeller, values of k^* are at least one order of magnitude lower than the maximum. Larger values of k^* are found in the lower half of the vessel, close to the shaft, where the velocity (see Figs. 2(a) and (b)) is larger.

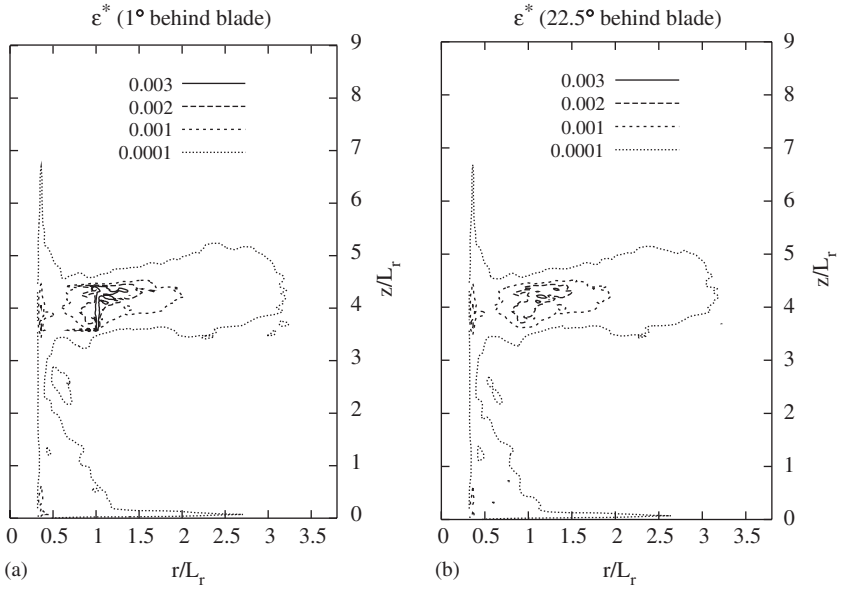

Fig. 4. Isocontours of angle-resolved averages of turbulent energy dissipation rate. Values are made dimensionless using the reference time and velocity scales ($\varepsilon^* = \varepsilon/(\Omega^3 L_r^2)$). Vertical sections are taken (a) 1° behind the impeller blade, and (b) mid-way between two blades.

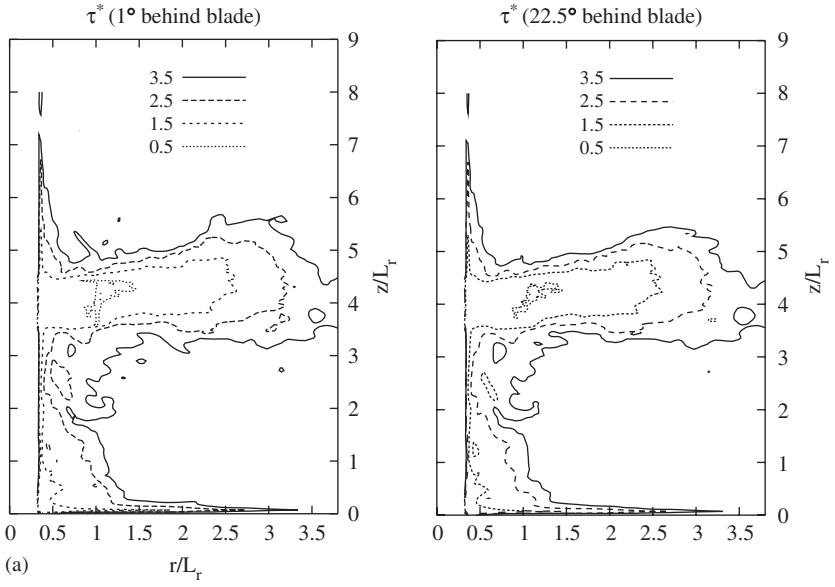

Fig. 5. Isocontours of dimensionless, angle-resolved averages of the dissipation relevant time-scale, $\tau^* = \Omega\tau$. Vertical sections aree taken (a) 1° behind the impeller blade, and (b) mid-way between two blades.

Comparison of Figs. 3(a) and (b) indicates no significant variations of turbulent kinetic energy distribution in the azimuthal direction. This was expected, since the number of blades is relatively high (8).

Fig. 4 shows the distribution of turbulent energy dissipation rate, ε, calculated as

$$\varepsilon = 2\nu S_{ij} S_{ji}, \tag{2}$$

where, S_{ij} is the strain tensor, i.e., the symmetric part of the velocity gradient tensor, and values are made dimensionless using $\varepsilon^* = \varepsilon/(\Omega^3 L_r^2)$. The vertical sections are the same shown in Figs. 3(a) and (b). The spatial distributions of k^* and ε^* are qualitatively similar, with peak values at the blade tip. We then used the values of k^* and ε^* to calculate the spatial distribution of the relevant time-scale of the dissipative scales as $\tau = (\nu/\varepsilon)^{1/2}$. This will be the smallest flow time-scale and will be significant to determine particle behavior. Fig. 5 shows values of τ, made dimensionless using $1/\Omega$, ($\tau^* = \Omega\tau$). Similarly to Figs. 3 and 4, values of τ^* are angle-resolved averages obtained for (a) a vertical plane one degree behind the blades, (b) a vertical plane mid-way between two blades. The smallest

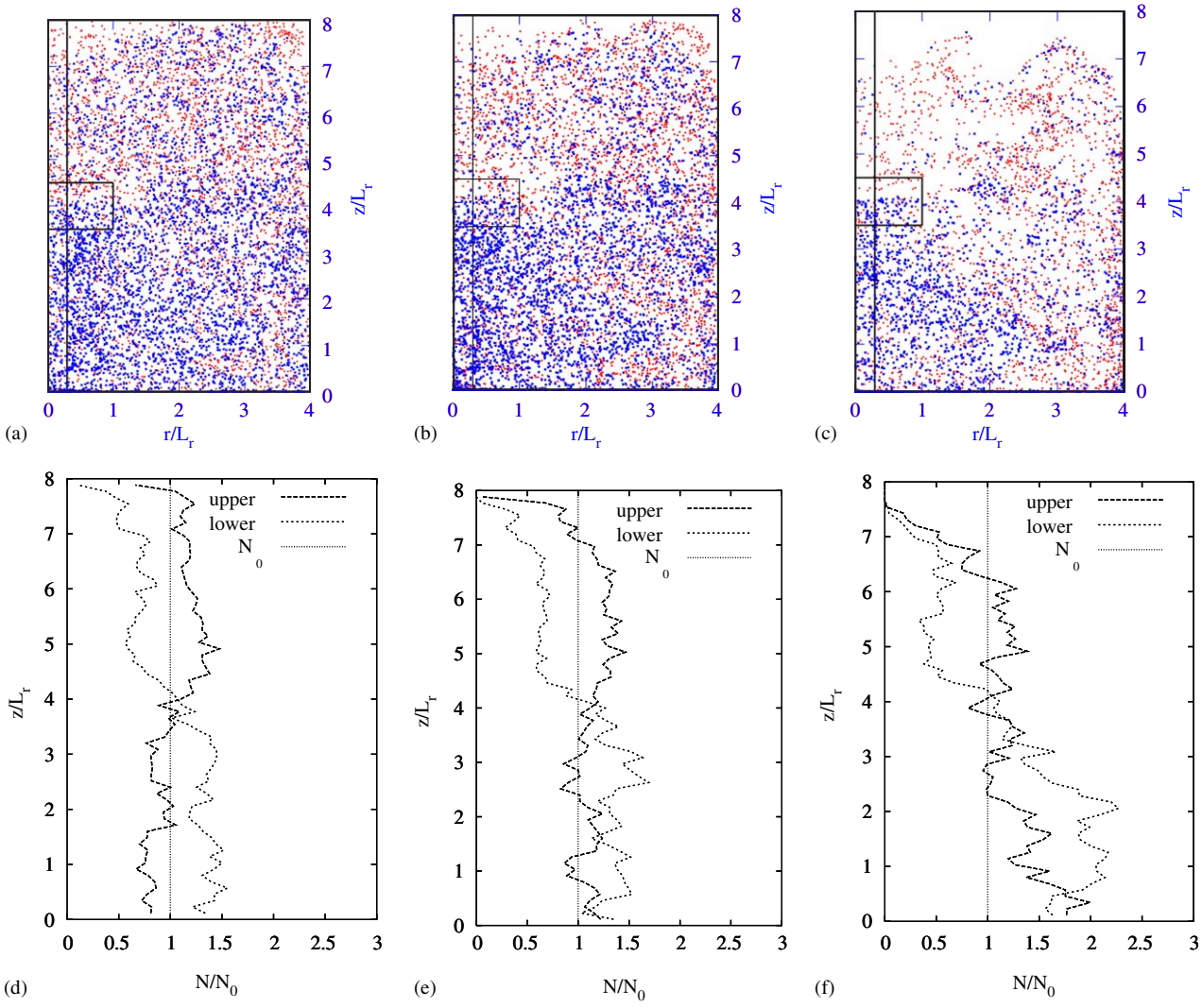

Fig. 6. Snapshots of instantaneous particle position after three impeller revolutions for particles released above (red) and below (blue) the impeller mid-plane: (a) 30 μm particles, (b) 50 μm and (c) 100 μm. Vertical profile of particle concentration for (d) 30 μm, (e) 50 μm and (f) 100 μm particles released above and below the impeller.

values of τ^* are found near the blade tip where the larger dissipation rate is also observed in Fig. 4. Values of τ^* increase progressively moving outward, along the radial direction. The dimensionless isocontours near the blade tip correspond to a time-scale $\tau < 5\times10^{-2}$ s which is one order of magnitude larger than the value calculated a priori in the Methodology section (2.35×10^{-3} s). These results will be useful to comment on particle segregation data.

3.2. Particle distribution

We performed our Lagrangian simulations considering a particle-to-fluid density ratio equal to $\rho_p/\rho = 5$ and particle diameters equal to 30, 50 and 100 μm. These particles are expected to settle down under gravity if the stirring action is not effective. To get some insight on the influence of the injection point on the dispersion and settling process, for each diameter we consider two swarms of 2×10^4 particles randomly distributed above and below the impeller plane ($z = L_H/2$) at starting time. Figs. 6(a)–(c) show the instantaneous distribution of particles after three impeller revolutions. A thin slice of the reactor taken in correspondence of the blade position is considered for visualization. Red particles are those released in the upper half of the vessel, blue particles are those released in the lower half. After three revolutions, 30 μm particles are still homogeneously dispersed in the vessel, 50 μm particles show a mild tendency to move downward under the effect of gravity and this effect becomes predominant for the 100 μm particles, which eventually have left the upper part of the vessel. This is shown more clearly in Figs. 6 (d)–(f), showing the vertical profile of concentration for upper and lower particles. At starting time, the concentration was $N/N_0 = 2$ in the upper half of the vessel and 0 in the lower half for red particles, and $N/N_0 = 0$ in the upper half of the vessel and 2 in the lower half for blue particles.

Table 2
Average value and standard deviation of the circulation path lengths, c, calculated for all particle diameters

Particle diameter (μm)	Initial position	Average $[L_r]$	Standard deviation $[L_r]$
30	Upper	13.644	3.509
30	Lower	13.614	4.114
50	Upper	13.370	3.466
50	Lower	12.688	4.726
100	Upper	12.603	3.204
100	Lower	9.483	4.818

Values are made dimensionless using the impeller blade radius L_r.

Consider first 30 μm particles (Fig. 6(d)). After three revolutions, 50% of the red particles has moved in the lower half and 50% of the blue particles has moved upward. This balance modifies for larger particles, due to the growing effect of gravity. For 100 μm particles (Fig. 6(f)), the number of particles moving downward is larger than the number of particles moving upward.

Trajectories analysis (figure not shown here) reveals that the smaller (30 μm) particles tend to circulate over the entire domain being easily resuspended by the upward flow, whereas 50 and 100 μm particles gradually move toward the lower part of the reactor. Specifically, for 50 μm particles settling is delayed thanks to a quasi-equilibrium between drag and gravity obtained some vertical distance apart from the bottom wall. For 100 μm particles, no equilibrium region is observed.

3.3. Circulation time statistics

Analyzing particle distribution in the vessel is useful to identify high/low dispersion regions. Yet, it gives no information on dispersion dynamics, i.e., the traveling distance of particles inside the vessel. To this purpose, we calculate the length of particle trajectories over the entire Lagrangian tracking simulation (3 impeller revolutions) for particles initially released above and below the impeller plane (*upper* and *lower particles*, respectively).

We should recall here that the two macroscopic flow motions characterizing unbaffled stirred tanks are (i) a circular bulk rotation of the flow around the axis of the tank and (ii) a top–bottom recirculation, induced by the impeller discharge jet. In the 3-D domain, these correspond to two recirculation regions, above and below the impeller plane, having the shape of toroidal vortices. The circular bulk rotation is most similar to a solid-body rotation and does not affect mixing, whereas top–bottom recirculation produces transfer in the axial direction and is crucial for mixing processes. Therefore, to eliminate the bulk flow effect from our analysis, we evaluated the length of the *recirculation path* integrating the axial and radial (Δr and Δz) displacements along the entire Lagrangian simulation. The probability density functions of r–z circulation length, c, are shown in Fig. 7 for all particle diameters. Statistics on 2-D circulation lengths are given in Table 2.

For the upper particles, the mean value of circulation length decreases slightly as the particle size increases (see Figs. 7(a)–(c), top). For the lower particles, the circulation length distribution is broader and the mean value of circulation length decreases significantly as the particle size increases. Differences in the mean value of the circulation length arise from the joint contribution of gravitational settling and impeller pumping action which are in the opposite direction in the region above the impeller and in the same direction in the region below the impeller. Differences in the values of the standard deviation are most likely due to the larger values of rms velocity fluctuations of the fluid found in the region below the impeller, which may enhance differences in particle trajectories. Statistics shown in Table 2 indicate that the largest, 100 μm particles are characterized by very low circulation lengths—the average value is about $9.483L_r$, whereas the most probable value is about $3L_r$. In the lower part of the vessel, heavy particles tend to be trapped into low-velocity circulation regions which are unable to re-suspend particles toward the high mixing region around the impeller.

3.4. Particle preferential concentration

The ability of specific flow structures to capture particles and to form clusters is generally undesired in dispersion processes and a thorough understanding of this type of segregation is crucial for dispersion optimization (Campolo et al., 2005). Therefore, we tried to quantify the degree of preferential concentration in different regions of the tank using the same integral parameter used by Fessler et al. (1994), which quantifies the maximum deviation from randomness of the particle number concentration distribution.

In this work, we evaluate the degree of preferential concentration (a) in the impeller region, corresponding to a cylinder ($3L_r$ high) containing the impeller and (b) in the bottom of the tank. We divided these regions into small control volumes and counted the number of particles in each box, N_p, to calculate the particle number concentration. When the particles are randomly distributed, the PDF of N_p is Poisson type. If particles accumulate into specific regions, the PDF of N_p deviates from Poisson. Deviation from Poisson distribution is evaluated as:

$$D = \frac{\sigma - \sigma_{\text{Poisson}}}{\lambda}, \tag{3}$$

where σ is the variance of the calculated PDF, σ_{Poisson} and λ are the variance and the mean of the reference Poisson distribution. The largest is the value of D, the largest is the preferential accumulation of particles.

Fig. 8 shows results obtained for D when the box size is optimized to maximize D. Statistics are shown again for upper and lower particles. We observe that 100 μm particles exhibit the largest segregation, both in the impeller region and in the bottom of the tank, and the absolute value of D is larger in the bottom region. As observed previously, larger particles seem to be trapped due to the action of gravity into low flow circulation regions. Fessler et al. (1994) found that the preferential accumulation is maximum when the particle relaxation time is

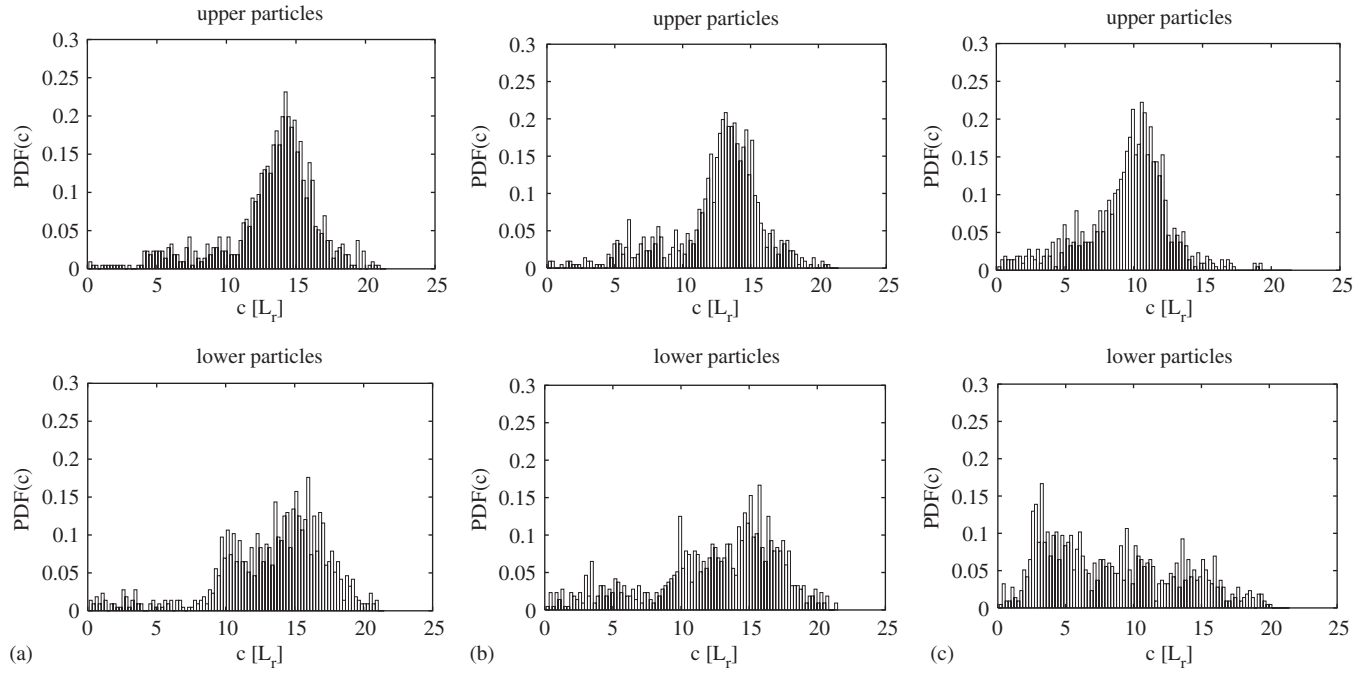

Fig. 7. PDF of 2-D trajectory length for (a) 30 μm, (b) 50 μm and (c) 100 μm particles. Statistics obtained for particle released above (top) and below (bottom) the impeller.

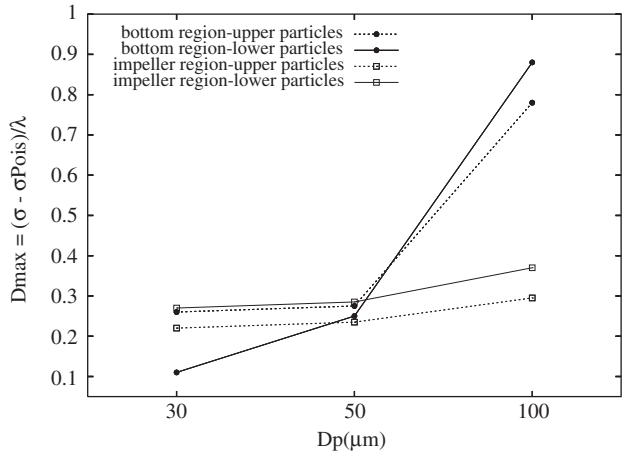

Fig. 8. Integral measure of preferential particle concentration for different size particles. Statistical values are calculated in the region around the impeller and in the lower half of the tank for particles released in the upper half and in the lower half of the vessel.

of the same order as the fluid time-scale which controls dispersion. In our case, τ_p of the 100 μm is closer to the estimated Kolmogorov time-scale, than τ_p of the 50 and 30 μm particles (see Table 1), indicating that this scale may play a significant role in particle segregation.

4. Conclusions

In this work we investigated the dispersion of small particles in a stirred tank using DNS to solve the flow balance equations down to the smallest scales (i.e., the Kolmogorov scales) and a Lagrangian approach to simulate the behavior of three swarms of 30, 50 and 100 μm diameter particles randomly dispersed in the vessel.

Preliminary results show that the structures dominating the flow are the radial discharge jet issued from the impeller and the top–bottom recirculation regions. The discharge jet divides into two opposite streams in correspondence to the wall generating two counter-rotating toroidal vortices above and below the impeller, responsible for the top–bottom recirculation and for the resuspension of settling particles.

Particle dispersion results show that, after three impeller revolutions, smaller (30 μm) particles remain quite randomly dispersed, behaving almost as fluid tracers, whereas migration is observed for 50 and 100 μm particles toward the bottom of the vessel. Analysis of particle trajectories showed that 50 μm particles reach an equilibrium region some distance above the bottom wall from which they can be resuspended in the flow, whereas 100 μm particles settle at the bottom and remain there. Measures of the 2-D radial–vertical circulation confirm the tendency of heavier particles to collect in the lower part of the reactor, accumulating into low velocity flow regions.

Integral measurements of particle preferential distribution indicate that 100 μm particles have maximum segregation, their time-scale being closer to the relevant time-scale of the flow field (Wang and Maxey, 1993; Eaton and Fessler, 1994).

Acknowledgements

Financial support from MIUR under contract RBAU01-NZH7_007 (FIRB) is gratefully acknowledged. One of us (RV) wishes to acknowledge the CEMeC for the support received during this study.

References

Campolo, M., Sbrizzai, F., Soldati, A., 2003. Time-dependent flow structures and Lagrangian mixing in Rushton-impeller baffled-tank reactor. Chemical Engineering Science 58, 1615–1629.

Campolo, M., Salvetti, M.V., Soldati, A., 2005. Mechanisms for microparticle dispersion in a jet in crossflow. A.I.Ch.E. Journal 51 (1), 28–43.

Chung, J.N., Troutt, T.R., 1988. Simulation of particle dispersion in an axisymmetric jet. Journal of Fluid Mechanics 186, 199–222.

Derksen, J.J., 2003. Numerical simulation of solids suspension in a stirred tank. A.I.Ch.E. Journal 49 (11), 2700–2714.

Derksen, J.J., Van den Akker, H., 1999. Large-eddy simulation on the flow driven by a Rushton turbine. A.I.Ch.E. Journal 45, 209–221.

Eaton, J.K., Fessler, J.R., 1994. Preferential concentration of particles by turbulence. International Journal of Multiphase Flow 20, 169–209.

Fadlun, E.A., Verzicco, R., Orlandi, P., Mohd-Yusof, J., 2000. Combined immersed-boundary/finite-difference methods for three-dimensional complex flow simulations. Journal of Computational Physics 161, 35–60.

Fessler, J.R., Kulick, J.D., Eaton, J.K., 1994. Preferential concentration of heavy particles in a turbulent channel flow. Physics of Fluids 6 (11), 3742–3749.

Kolmogorov, A.N., 1941. Dissipation of energy in a locally isotropic turbulence. American Mathematical Society Translations Series 2, vol. 8, Providence RI, p. 87.

Kuerten, J.G.M., Vreeman, A.W., 2005. Can turbophoresis be predicted by large-eddy simulation? Physics of Fluids 17 (1), 1–4.

Loth, E., 2000. Numerical approaches for motion of dispersed particles, droplets and bubbles. Progress in Energy and Combustion Science 26, 161–223.

Marchioli, C., Soldati, A., 2002. Mechanisms for particle transfer and segregation in a turbulent boundary layer. Journal of Fluid Mechanics 468, 283–315.

Maxey, R.M., Riley, J.J., 1983. Equation of motion for a small rigid sphere in a nonuniform flow. Physics of Fluids 26 (4), 883–889.

Picciotto, M., Marchioli, C., Soldati, A., 2005. Characterization of near-wall accumulation regions for inertial particles in turbulent boundary layers. Physics of Fluids 17, 098101.

Pope, S.B., 2000. Turbulent Flows. Cambridge University Press, Cambridge.

Rouson, D.W.I., Eaton, J.K., 2001. On the preferential concentration of solid particles in turbulent channel flow. Journal of Fluid Mechanics 428, 149–169.

Shotorban, B., Mashayek, F., 2005. Modeling sub-grid-scale effects on particles by approximate deconvolution. Physics of Fluids 17, 081701.

Soldati, A., 2005. Particles Turbulence Interactions in Boundary Layers. ZAMM 85, 683–699.

Verzicco, R., Fatica, M., Iaccarino, G., Orlandi, P., 2004. Flow in an impeller-stirred tank using an immersed-boundary method. A.I.Ch.E. Journal 50 (6), 1109–1118.

Wang, L.P., Maxey, M.R., 1993. Settling velocity and concentration distribution of heavy particles in homogeneous isotropic turbulence. Journal of Fluid Mechanics 256, 27–68.